

Asteroseismically Inferred Ages of 132,000 Red Giants with TESS

ARTEMIS THEANO THEODORIDIS,¹ LESLIE MORALES,¹ AND JAMIE TAYAR¹

¹*Department of Astronomy, University of Florida, USA*

ABSTRACT

NASA's TESS mission has identified at least 158,000 oscillating red giants, increasing the known sample by roughly an order of magnitude. After validating that these measurements are reliable to 5% for up to 90% of red giants (Theodoridis & Tayar 2023), we make custom stellar evolution models using MESA in order to estimate ages for \sim 132,794 of these stars to an average uncertainty of 23%. We show that these ages follow similar distributions to those observed in other samples such as Kepler with small differences likely resulting in the galactic volume probed. We provide these ages to the community to enable future galactic archaeology analyses.

Keywords: Red Giant Stars (1372) — Stellar Ages(1581) — Astronomy Data Modeling(1859) — Stellar Evolution (1599)

1. INTRODUCTION

Accurate calculations of stellar ages are integral to understanding the formation and evolution of our galaxy. Ages have been used to trace the evolution of the galactic bulge (Joyce et al. 2023), the thin and thick disks (Feuillet et al. 2022; Helmi et al. 2018), the halo (Mackereeth et al. 2018; Iorio et al. 2018), accreted dwarf galaxies (Grunblatt et al. 2022; Feuillet et al. 2022), as well as interactions between these components (Chaplin et al. 2020). These galactic archaeology studies have determined that the galaxy has different components and that they have evolved and interacted with each other over time. Having ages for these stars allows us to understand the chronological order of their evolution.

However, there are still two major challenges in this field: 1. In past decades, precise and accurate age interpolation and determination have been limited to small portions of the sky, which may not be generalizable to the full galaxy. 2. There are also disagreements on the age of each star depending on the model and methods chosen to derive said ages, which can impact the inferred galactic history (eg. Tayar & Joyce 2025). These limitations lead to the debate over the accuracy of individual studies and significant differences in derived ages for larger samples (e.g. comparing Silva Aguirre et al. 2018; Xiang & Rix 2022; Stokholm et al. 2023; Nataf et al. 2024).

Since ages are not a directly measurable property in most cases, almost all ages are derived in reference to a stellar model. However, numerous physical as-

sumptions must be made to construct a stellar model (Joyce et al. 2024) and many can impact the inferred age (Ying et al. 2023). In most commonly used models (Takeda et al. 2007), physics such as convective overshoot, helium abundances, atmospheric boundary conditions, and mixing length are heavily simplified. This can lead to different ages across studies for the same star depending on the stellar models used. Various studies explore the complexities of stellar modeling physics alongside their uncertainties (van Saders & Pinsonneault 2013; Choi et al. 2016; Joyce & Chaboyer 2018), and in general they find that much of the physics of stellar evolution is still truly uncertain at some significant level, and so even though individual authors are all making reasonable assumptions, they may predict slightly different evolution for the same star. While addressing these complex physical processes is a long-term ongoing effort, there are a significant number of cases where models agree quite well and can be used to draw interesting conclusions about the history of the galaxy.

In particular, work has been done to map the differences in inferred ages from different model grids (Tayar et al. 2022; Byrom & Tayar 2024; Morales et al. 2025). In general, ages can be uncertain to 20% for main-sequence and sub-giant stars and up to 80% for red giants. However, the age of a star is strongly related to its mass, and so when the mass of a star is directly measured or calculated, the discrepancy between models drops significantly. This is particularly relevant for red giant branch stars (Pinsonneault et al. 2025; Morales et al. 2025), where small changes in mass can lead to significant dif-

ferences in their inferred age. The large discrepancies between models when mass is unknown arise from the fact that models of different masses have very similar temperatures on the red giant branch, and so a slight shift in the model temperature can change the inferred mass significantly. Therefore, when estimating ages for samples of red giant stars, it is strongly preferable to choose stars where the stellar mass can be inferred directly. One of the best ways to get masses for large samples of single stars is asteroseismology.

Asteroseismology, the study of stellar oscillations, provides further knowledge of a star's internal structure and evolution (Brown et al. 1991; Kjeldsen & Bedding 1995). Oscillations within stars excite certain frequencies that are related to the bulk properties of the star. For stars with a solar-like structure, that is, a convective surface, turbulent convective motions will excite waves for which pressure is the restoring force. These modes will be excited at a range of frequencies, with an envelope of peaks that are roughly Gaussian, and a peak frequency that scales with the surface gravity of the star and is called the frequency of maximum power, or ν_{\max} . There will also be regular spacings between modes of the same spherical degree ℓ , which are called the large frequency spacing, or $\Delta\nu$, and this will scale with the mean density. Combining various stellar components such as ν_{\max} , $\Delta\nu$ and effective temperature allows for a calculation of the star's mass, which, in combination with a metallicity and a stellar model, can provide a more precise estimate of a star's age.

It was only recently that the Kepler mission made it possible to use this technique for moderate samples, i.e. tens of thousands of stars. Galactic archaeology goals need truly large data sets, more like hundreds of thousands or millions of stars. Many researchers have used machine learning to bridge the gap (Ness et al. 2016; Mackereth et al. 2019; Leung & Bovy 2019; Anders et al. 2023; Queiroz et al. 2023; Stone-Martinez et al. 2024) but this approach has some challenges. In particular, there are often difficulties with interpretability, identifying adequate and unbiased training sets, and mitigating edge-case inaccuracies (Tayar et al. 2023; Ting 2024). For both direct asteroseismic analysis and identifying training samples for machine learning approaches, NASA's Kepler (Borucki et al. 2010) is almost unanimously considered the gold standard for asteroseismic samples because of its 4-year long continuous observation of the same part of the sky, allowing detailed measurements of frequencies that are well resolved in the Fourier domain. That said, this sample is somewhat limited by its small field of view and the specific population of stars available in that part of the sky. Despite

the relatively small sample size, incredible advancements have been made in the study of galactic archaeology using machine learning trained on this small sample of a few thousand stars. For example, nearly 100,000 stellar ages have been inferred using machine learning methods trained on asteroseismic results on large spectroscopic surveys, and detailed maps have been made of the evolutionary history of the Milky Way (Ness et al. 2016; Leung & Bovy 2019; Anders et al. 2023; Queiroz et al. 2023; Stone-Martinez et al. 2024).

Although these measurements have significantly advanced the field of galactic archaeology, NASA's TESS (Transiting Exoplanet Survey Satellite)(Ricker et al. 2010) has the potential to drastically increase the number of asteroseismic ages available. TESS is an all-sky survey that includes millions of observed red giants (Mackereth et al. 2021; Hatt et al. 2024; Zhou et al. 2024), 158,000 of which are confirmed identified oscillators (Hon et al. 2021). In the Hon et al. (2021) article specifically, machine learning was used to identify potential red giant oscillators and estimate a frequency of maximum power. Combining that ν_{\max} with a stellar radius estimate from Gaia and either a photometric or spectroscopic temperature estimate is sufficient to compute a seismically-informed mass. Previous work (Theodoridis & Tayar 2023) has shown that TESS seismology is calibrated to the Kepler scale to better than 5% for about 90% of red giants, indicating an excellent agreement to data that is considered a gold standard and capability for future studies. This allows us to address the two problems mentioned earlier:

1. We are no longer limited to a small field of view in our data since TESS has looked at almost the whole sky over the course of its mission.
2. These ages come from stars of constrained mass, which reduces the model-dependent systematics in red giant ages from $\sim 80\%$ percent to $\sim 10\%$ (Morales et al. 2025).

This allows us to provide a more direct age estimate for a very large sample of stars, which can then be used for galactic archaeology studies, contributing to our understanding of the formation and evolution of the Milky Way and its red giant stellar populations. We also hope that this sample can be used to identify interesting stars or subsample for more detailed individual studies of interesting objects in the future, although we do not attempt such studies here.

2. DATA

While it is in some cases possible to estimate ages of stars from their temperatures, luminosities, and metallicities (Nataf et al. 2024; Xiang & Rix 2022; Godoy-Rivera et al. 2021, etc.) work done by Morales et al.

(2025) has shown that such ages for giant stars depend significantly on the stellar models used. However, ages estimated from the stellar mass and metallicity are much less sensitive to the chosen model. Therefore, we define a set of stars where we can estimate mass, metallicity, and surface gravities on the red giant branch from a combination of TESS and Gaia data.

2.1. TESS Seismology

Work done by Hon et al. (2021) identified 158,000 oscillating red giants from TESS data, which we focus on in this study. The construction of the TESS Catalog utilized deep learning, a form of supervised machine learning, which was initially applied to Kepler/K2 data to detect red giant oscillators and estimate ν_{\max} values with performance comparable to human experts (Hon et al. 2018). This technique involved two independently trained convolutional neural networks that analyzed 2D images of power spectra, effectively “visually” identifying red giant oscillation signatures.

This method was applied to TESS data, analyzing long-cadence photometry taken at 30-minute intervals for one month (27 days). Using data from the MIT Quick-Look Pipeline (Huang et al. 2020, QLP), which extracts light curves from Full Frame Images (FFI), the analysis led to the identification of oscillations in approximately 158,000 red giants over the TESS two-year primary mission (Years 1 and 2, Cycles 1–26).

The best seismology available to date (e.g. Lund et al. 2017; Zinn et al. 2019; Schonhut-Stasik et al. 2023; Pinsonneault et al. 2025) comes from extensive datasets with long observation times and careful analysis by many researchers. For this reason, the use of machine learning on short datasets has faced skepticism. However, the TESS data have been validated through comparison with independent asteroseismic pipelines in well-studied regions, including stars that were independently observed by both the TESS and Kepler missions (Stello et al. 2022). TESS studies in the southern continuous viewing zone using multiple techniques were also found to be in good agreement with each other (Mackereth et al. 2021), suggesting that the TESS data in itself is of high quality for asteroseismic analyses.

Additionally, machine learning seismic ν_{\max} values were found to be consistent with spectroscopically calibrated ν_{\max} values on the Kepler scale (Theodoridis & Tayar 2023). Across various studies, the ν_{\max} values were found to agree well with those from external analyses (Mackereth et al. 2021; Stello et al. 2022; Hatt et al. 2022), reinforcing the reliability of their use in our sample. While these ν_{\max} measurements are based on 1 sector, those with multi sector detections show a

97% agreement rate between sectors, suggesting that the short datasets used are sufficient.

These studies together indicate that the Hon et al. (2021) ν_{\max} values are reliable, and therefore we follow Stello et al. (2008) and Hon et al. (2021) to estimate masses using the following equation:

$$\frac{M}{M_{\odot}} = \left(\frac{\nu_{\max}}{\nu_{\max,\odot}} \right) \left(\frac{R}{R_{\odot}} \right)^2 \left(\frac{T_{\text{eff}}}{T_{\text{eff},\odot}} \right)^{0.5},$$

with $\nu_{\max,\odot} = 3090 \mu\text{Hz}$ (Huber et al. 2011) and $T_{\text{eff},\odot} = 5771.8 \text{ K}$ (Prša et al. 2016).

While the agreement is satisfactory, caveats exist for the method of ν_{\max} determination. Blending remains a potential issue, particularly for stars with similar ν_{\max} values (Hon et al. 2021). Fainter targets are at the greatest risk of blending.

2.2. Gaia Radii

Because we do not have seismic $\Delta\nu$ values, we require an additional constraint to estimate masses. We use radii from Hon et al. (2021) computed using `isoclassify` (Huber et al. 2017; Berger et al. 2020, 2023) that uses parallaxes from Gaia EDR3 (Gaia Collaboration et al. 2021) as an input. To eliminate blended targets and specify isolated ones, they required that each target have an effective temperature (T_{eff}) and radius (R) that are similar to those of an oscillating red giant.

2.3. Spectroscopic Sample and Calibration

2.3.1. XGBoost

The Gaia mission (Gaia Collaboration et al. 2016, 2018), renowned for its precise astrometry and photometric measurements, also provides spectroscopic data through its Radial Velocity Spectrometer (RVS) and low-resolution XP spectra. The short-wavelength spectra are referred to as “blue photometer” (BP) spectra, while the long-wavelength spectra are known as “red photometer” (RP) spectra. XP spectra is used to collectively refer to both types of Gaia spectra. The RVS operates at a resolution of ~ 8000 around the near-infrared Ca triplet, enabling the measurement of radial velocities and contributing to our understanding of Galactic dynamics. Additionally, XP spectra, obtained via BP and RP prisms, span wavelengths from 350 to 1000 nm but have limited resolution ($R \sim 40$ –150), posing challenges for deriving precise metallicities ([M/H]). To address these limitations, a data-driven approach using the machine learning algorithm XGBoost was employed (Andrae et al. 2023) to estimate stellar parameters such as [M/H], effective temperature (T_{eff}), and surface gravity ($\log g$). The XGBoost model was trained on high-fidelity datasets, including APOGEE DR17 (see

Section 2.4), which provides stellar parameters for stars with well-characterized metallicities. Training features incorporated XP spectral coefficients, GaiaXP-derived synthetic photometry (e.g. [Gaia Collaboration \(2022\)](#)), broadband magnitudes, and parallaxes, effectively mitigating degeneracies, such as those between T_{eff} and dust reddening. By leveraging these features and augmenting the training set with metal-poor stars, XGBoost delivers robust metallicity estimates across a wide range of stellar types and magnitudes, demonstrating its potential as a powerful tool for deriving metallicities in stellar populations.

We employ a crossmatch between the Gaia DR3 dataset and our TESS-identified red giants, creating a catalog of 134,901 stars that includes both TESS seismology and Gaia-derived radii and metallicities.

2.4. APOGEE

For further calibration and validation of the XGBoost parameters, we employ spectroscopic parameters from the Apache Point Observatory Galactic Evolution Experiment (APOGEE DR17 [Abdurro'uf et al. \(2022\)](#)) run as part of the SDSS-III/APOGEE and SDSS-IV/APOGEE-2 surveys ([Majewski et al. 2017](#)). These spectra offer estimates of parameters such as effective temperature, metallicity, and surface gravity that are higher precision and accuracy than those derived from the Gaia data, which provides reduced uncertainties in our derived masses and ages. We can use the subset of stars with available APOGEE data to validate and calibrate our mass and age estimates, along with their associated uncertainties.

The APOGEE Stellar Parameters and Chemical Abundances Pipeline (ASPCAP, [García Pérez et al. 2016](#); [Holtzman et al. 2018](#); [Jönsson et al. 2020](#)) processes the spectroscopic data using the Synspec atmospheric models ([Hubeny & Lanz 2017](#); [Hubeny et al. 2021](#)). This automated pipeline provides near-infrared spectra and derives stellar parameters such as effective temperature (T_{eff}), surface gravity ($\log g$), and metallicity ($[M/H]$). Additionally, it determines elemental abundances for up to 20 species.

Comparisons in clusters ([Sinha et al. 2024](#)) and external validation data ([Pinsonneault et al. 2025](#)) suggest that the uncertainties on the abundances and stellar parameters are small, although there may be some residual trends at the 0.03 dex level with temperature and gravity ([Sinha et al. 2024](#)).

Because these data have been extensively processed and validated, many low-level trends and offsets have been documented. Potentially relevant to our study, we note that the APOGEE gravities for clump stars show a

slight correlation between (T_{eff}) and $\log g$ at the 0.18 dex per 1000 K level ([Chen et al. 2015](#); [Holtzman et al. 2015](#)) and APOGEE gravities for stars with $[M/H] < -1.5$ dex may be offset by 0.2 dex from optical results ([Jönsson et al. 2018](#)).

2.5. Entire Sample

For our sample, we follow the procedure of [Theodoridis & Tayar \(2023\)](#) to combine Gaia, TESS, and XGBoost to estimate seismically-informed masses and surface gravities for each of our red giants.

The cross-match occurs through a Python script utilizing the `astropy` table function, ensuring proper correspondence of stellar IDs between the applicable datasets. Specifically, we used the correspondence between `TIC_ID` from TIC-v8 ([Stassun et al. 2019](#)) and `gaiadr3_source_id` and eliminated any stars that did not have a matching counterpart across the individual datasets. Once this cross-match was completed, we were left with 134,901 red giant stars out of the 158,014 red giant oscillators detected in our TESS sample.

We added to our table calculations of seismic $\log(g)$ and mass in a similar fashion to [Hon et al. \(2021\)](#), using GAIA EDR3 radius ([Hon et al. 2021](#)), XGBoost (T_{eff}), and ν_{max} ([Hon et al. 2021](#)) to combine these different datasets and estimate seismically-informed masses and surface gravities for all 134,901 stars in our sample. We used the APOGEE DR17 sample as an additional check to validate our choice of effective temperature and $[M/H]$ parameters. For the $\sim 12,000$ stars where APOGEE parameters were available, we compared the (T_{eff}) and $[M/H]$ values with those from XGBoost (Figure 2) versus [Hon et al. \(2021\)](#). Figure 1 shows the HR diagram positions, as well as the mass and metallicity distributions, for the full sample.

The determination of error bars for the seismic $\log(g)$ and the mass was calculated using standard equations for error propagation, and the average errors are 12% for mass and 5% for seismic $\log g$. These results can be found in Table 2.

2.6. Data Validation

In general the frequency of maximum power, ν_{max} , is expected to scale with the surface gravity and temperature of the star. We also note that the temperature values from XGBoost generally agree with the APOGEE temperatures better than the temperature values inferred using `isoclassify` in [Hon et al. \(2021\)](#) (see Figure 2), and therefore we use the XGBoost temperatures in our calculations.

3. MODELING GRID

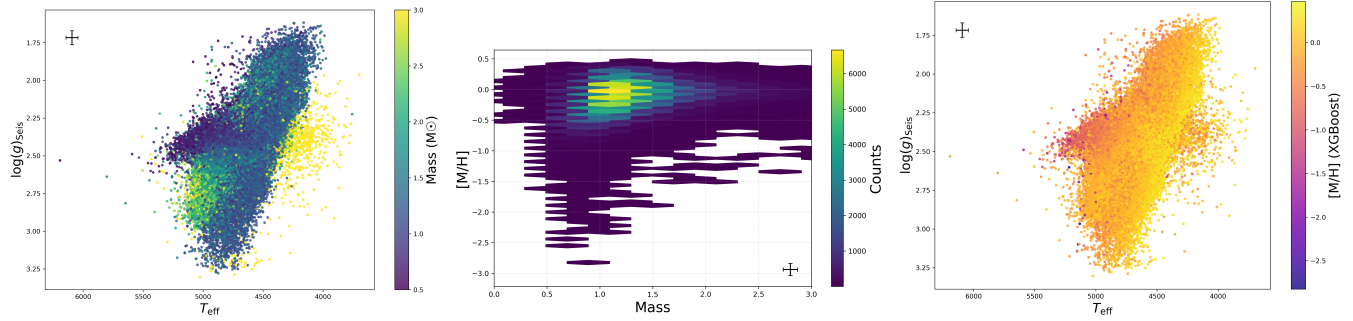


Figure 1. We present two HR diagrams of our sample, showing the relationship between seismic surface gravity ($\log(g)_{\text{seis}}$) and XGBoost effective temperature (T_{eff}), color-coded by metallicity (right) and mass (left). The middle plot shows the density distribution of the sample, highlighting the range of stellar masses and metallicities. We also note that the population of very cool, apparently high-mass ($> 3 M_{\odot}$) yellow stars in the left panel are likely to be spurious, and not genuine rapidly rotating or spotted massive merger products. In general, we observe that giants near solar metallicity span a range of masses, while lower metallicity stars tend to be lower mass, and no giants exceed a metallicity of approximately $[M/H] \sim 0.5$. These plots provide a detailed overview of our sample’s distribution across these key parameters. The cross in the corner of each plot represents the average uncertainty across each axis.

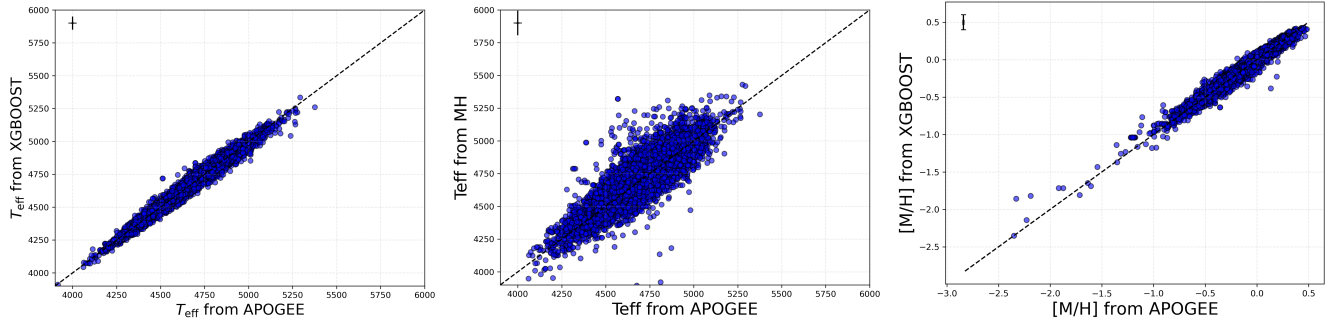


Figure 2. Comparisons between the parameters inferred from APOGEE, and those inferred from Gaia. In particular, we find that the XGBoost temperature scale (left) is closer to the APOGEE temperature scale than the temperatures computed in Hon et al. (2021) (middle). We also find that the XGboost metallicities agree with the APOGEE scale to better than 0.03 dex in the majority of cases (right panel) thus validating their use in our age calculations. The cross located in the top right corner of each plot represents the average uncertainty across each axis, with the (T_{eff}) error from XGBoost being uniformly 50K.

Our modeling framework employs MESA (Modules for Experiments in Stellar Astrophysics), version r22.11.1 (Paxton et al. 2011, 2013, 2015, 2019; Jermyn et al. 2023), to construct a comprehensive grid of stellar models tailored to the properties of low-mass red giants. This version adds automatic differentiation to MESA, improving model precision and efficiency. It enhances energy equation accuracy, and updates treatments of opacities, element diffusion, and nuclear reactions. MESA’s adaptive mesh refinement and advanced time-stepping algorithms allow it to handle a broad range of stellar evolution scenarios (binary systems, binary mergers, mass loss, mass transfer, rotation, etc.), making it an ideal choice for simulating red giant evolution across diverse metallicities and other stellar parameters such as age, mass, and $\log g$. The MESA models are particularly robust in calculating evolution-

ary tracks for low-mass stars, from the zero-age main sequence (ZAMS) through to the asymptotic giant branch (AGB) phase. In particular, MESA solves the one-dimensional stellar-structure and composition equations for each star we model. We use MESA as it is capable of running through the helium flash consistently, which is needed for our grid and age interpolation. Processes for mixing and burning are solved simultaneously, and discussion of specific stellar input physics are described below.

We have constructed our own modeling grid as follows:

$$\begin{aligned} M_{\text{init}} &= \{0.7, 0.8, \dots, 3.0\}, \\ [\text{Fe}/\text{H}]_{\text{init}} &= \{-2.0, -1.9, \dots, +0.5\} \\ Z_{\text{init}} &\in \{0.000179492, 0.000225967040014, \\ &\quad 0.000284475648901, 0.000358133623438, \\ &\quad 0.000450863519365, 0.000567603541779, \\ &\quad 0.00071457052257, 0.000899590989382, \\ &\quad 0.00113251795675, 0.00142575563507, \\ &\quad 0.00179492, 0.00225967040014, \\ &\quad 0.00284475648901, 0.00358133623438, \\ &\quad 0.00450863519365, 0.00567603541779, \\ &\quad 0.0071457052257, 0.00899590989382, \\ &\quad 0.0113251795675, 0.0142575563507, \\ &\quad 0.0179492, 0.0225967040014, \\ &\quad 0.0284475648901, 0.0358133623438, \\ &\quad 0.0450863519365, 0.0567603541779\}. \end{aligned}$$

for a total of $24 \times 26 = 624$ models in our grid. Our Y_i is scaled according to Z_{init} via the canonical relation

$$Y_i = Y_0 + \frac{\Delta Y}{\Delta Z} \times Z_i, \quad (1)$$

where Y_0 is the primordial He abundance and $\frac{\Delta Y}{\Delta Z}$ is the He-to-metal enrichment ratio. We take $Y_0 = 0.2454$ (Planck Collaboration et al. 2020) and $\frac{\Delta Y}{\Delta Z} = 1.5137$.

3.1. Adopted Stellar Physics

We used a simplified version of the input physics described in Joyce et al. (2024) to construct a grid with updated physics specifically tailored to the mass and metallicity range present in our sample, focusing on the factors most likely to significantly impact the inferred ages of red giants. The metallicity range in our grid is set based on the distribution we found in our completed cross-matched dataset between GAIA, APOGEE, and TESS as detailed in the previous sections. The percentage of models that reached the red giant branch tip of their evolution is roughly 93% percent. With efficiency of model run-time in mind, our models were truncated with a maximum of 24 hours in run-time, giving just enough time to reach and fully fit the evolution of low-mass red giant stars up to the helium flash. Out of all the models ran in the original grid, there was a systematic error in the [Fe/H] value of 0.3, where the model failed across all masses. In our finalized grid, we implemented a value of 0.299 instead, and had greater success with only 5 models failing. With the failing tracks excluded, our grid consists of 619 models in total.

We show in Table 1 a synopsis of the input physics included in our models, and include a sample `inlist.inlist_common` file in Appendix B. In particular, we assume a Grevesse & Sauval (1998) solar mixture, the Eddington grey $T-\tau$ relation for atmospheric boundary conditions (Eddington 1930), and the Henyey mixing length scheme (Henyey et al. 1964) with a fixed value of $\alpha_{\text{MLT}} = 1.94$ based on solar calibration in our grid (see section 3.2). For high temperature opacities we used the OPAL (Rogers et al. 1996) tables with the appropriate GS98 mixture, and for low temperatures we used the (Ferguson et al. 2005) opacities with the appropriate GS98 mixture in order to produce more accurate predictions for low-temperature giants. The models utilize the `pp_extras.net`, `co_burn.net`, and `approx21.net` nuclear reaction networks. In particular, `approx21` nuclear reaction network, consists of 21 species: ^1H , ^3He , ^4He , ^{12}C , ^{14}N , ^{16}O , ^{20}Ne , ^{24}Mg , ^{28}Si , ^{32}S , ^{36}Ar , ^{40}Ca , ^{44}Ti , ^{48}Cr , ^{52}Fe , ^{54}Fe , ^{56}Fe , ^{56}Ni , protons, and neutrons. We use the Reimers and Blöcker schemes for cool RGB and AGB winds, respectively (Reimers 1975; Blöcker 1995). We employ a value of $\eta_{\text{Reimers}} = 0.2$ (Miglio et al. 2012) for the Reimers RGB wind scheme. For the Blöcker wind scheme (Blöcker 1995), we adopted a value of $\eta_{\text{Blöcker}} = 0.01$, similar to (Choi et al. 2016, Mesa Isochrones and Stellar Tracks, MIST). We use the Schwarzschild criterion for convective stability (Anders et al. 2023) and since we use the Schwarzschild criterion, we do not account for thermohaline mixing or semiconvection. Rotation is neglected because it does not significantly affect age interpolation results for red giants. Furthermore, we focus solely on single-star evolutionary calculations.

We describe how these mass loss choices compare to empirically calibrated mass loss rates in Section 4, and describe our final mass loss assumptions for clump stars there.

3.2. Modeling Procedure

To perform a solar calibration, we varied the mixing length and helium abundances until the solar mass ($1.00 M_{\odot}$) and solar metallicity ($z=0.0179492$) model matched the solar temperature (5772K, Prša et al. 2016) and solar luminosity ($L_{\text{sun}} = 3.8270 \times 10^{33} \text{ erg s}^{-1}$) at the solar age (4.57 Gyrs, Bahcall et al. 2006).

We show our tracks for a range of masses at solar metallicity in Figure 3 for reference.

4. AGE INTERPOLATION

Our primary goal is to estimate the ages of stars to further our understanding of stellar evolution. To

Table 1. Summary of the Input Physics Used in Our Model Grids Compared to Joyce et al. (2024).

Parameter	Grid	Joyce
Atmosphere	Eddington (1930)	Eddington (1930)
α -enhancement	None	None
Convective Overshoot	diffusive $f_{\text{core}} = 0.016$, $f_{\text{env}} = 0.0174$ (Choi et al. 2016)	None
Diffusion	None	None
Equation of State	OPAL+SCVH+MacDonald+HELM+PC	OPAL+SCVH+MacDonald+HELM+PC
High-Temperature Opacities	OPAL Rogers et al. (1996)	OPAL Iglesias & Rogers (1996)
Low-Temperature Opacities	Ferguson et al. (2005)	\AA SOPUS Marigo & Aringer (2009)
Mixing Length	1.94	1.931
Mixture	Greveste & Sauval (1998)	Greveste & Sauval (1998)
Nuclear Reaction Rates	Kunz et al. (2002)	Paxton et al. (2018)
Weak Screening	Chugunov et al. (2007)	None
Scaling Factor	Reimers (1975) $\eta = 0.2$, Bloecker (1995) $\eta = 0.01$	Blöecker (1995) $\eta = 0.01$
Solar X	0.7094815	0.7491
Solar Y	0.2725693	0.2377
Solar Z	0.0179492	0.0133
[M/H] Range	−2.0 to +0.5	−1.2 to +1.0
Mass Range	$0.7 M_{\odot}$ – $3.0 M_{\odot}$	1.0 to $5.0 M_{\odot}$

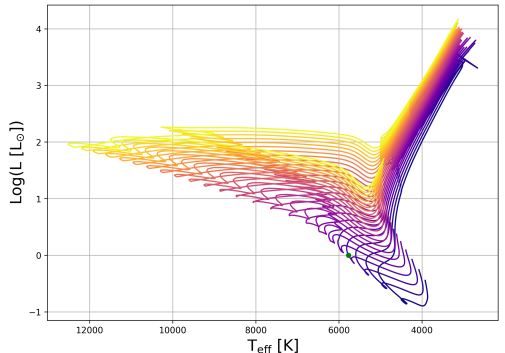


Figure 3. Stellar evolutionary tracks for various masses at solar metallicity in our grid. The tracks represent the evolution of stars from the pre-main-sequence (PMS) through the zero-age main sequence (ZAMS), the red giant branch (RGB), up to the clump. The blue dot represents the parameters of the sun, and the solar mass track goes through this point at the appropriate age.

achieve this, we use `kiauhoku`¹, an open-source package designed to interpolate stellar parameters from evolutionary model tracks (Claytor et al. 2020). `kiauhoku` enables custom grid installation, where we resample the model tracks into Equivalent Evolutionary Points (EEPs; Dotter 2016). Stellar parameters are then interpolated as a function of initial mass, metallicity, and EEP (Tayar et al. 2022), providing the initial guess for

a Nelder-Mead optimization (Nelder & Mead 1965) that minimizes a mean squared error loss function. The optimization is considered successful when it converges to a solution within a tolerance of 10^{-6} . We use a four-point interpolation scheme where possible. However, in regions where many evolutionary tracks fail to reach the tip of the giant branch, typically at low masses and high metallicities (i.e., old ages), we simplify to a two-point interpolation scheme to provide an estimate of age in as many stars as possible. We note that the heterogeneous spacing in age among tracks can introduce a ‘striping’ effect (see Figure 7), caused by the interpolation weight being biased toward the lower mass track. Specifically, for the interpolation, we use 1) mass derived from ν_{max} , Gaia R , and T_{eff} XGBoost, 2) surface gravity ($\log g$) computed from ν_{max} and XGBoost T_{eff} , and 3) metallicity from XGBoost. For clump stars, we adjust their masses to account for mass loss, as described in the previous section. Finally, we present the resulting age distribution in Figure 7, which shows the relationship between age and metallicity for both clump stars and first ascent giants.

We do not compute ages for stars with masses below $0.7 M_{\odot}$ even though such stars represent 1.2% of our sample (1623 stars). If we assumed that these objects had evolved as single stars, they would generally have ages significantly older than the universe. We expect that some of them are binary interaction products and some may be related to measurement errors but we consider detailed analysis of their properties outside the

¹ <https://github.com/zclaytor/kiauhoku>

Table 2. Table of our collected data and computed values including spectroscopic, Gaia-derived, and asteroseismic results, as well as derived masses and ages (see text for details). This table is available in its entirety in machine-readable form in the online article and on [Zenodo](#).

Label	Units	Contents
TIC	None	Stellar ID in TESS
Star_type	None	Recommended Evolutionary State
Final_age	Gyr	Age based on evolutionary state
ν_{max}	μHz	Frequency of Maximum power, Hon et al. 2021
Radius_gaia	R_\odot	Radius from Gaia, Hon et al. 2021
Teff_xgboost	K	T_{eff} from Gaia XGBoost
M_H_xgboost	dex	[Fe/H] metallicity from Gaia XGBoost
Logg_xgboost	cgs	Spectroscopic logg from XGBoost
Logg_seis	cgs	Seismic logg
E_Logg_seis	cgs	Uncertainty on seismic logg
Mass_seis	M_\odot	Seismic Mass
E_Mass_seis	M_\odot	Uncertainty on seismic mass
Initial_mass	M_\odot	Assumed initial mass of star accounting for empirical mass loss
Teff_rgb	K	Model temperature assuming RGB
Teff_rc	K	Model temperature assuming RC
Mean_age_rgb	Gyr	Mean age assuming RGB
Mean_age_rc	Gyr	Mean age assuming RC
Median_age_rgb	Gyr	Median age assuming RGB
Median_age_rc	Gyr	Median age assuming RC
E_age_rgb	Gyr	Standard deviation on RGB age
E_age_rc	Gyr	Standard deviation on RC age
E_lower_age_rgb	Gyr	Lower confidence interval RGB age
E_upper_age_rgb	Gyr	Upper confidence interval RGB age
E_lower_age_rc	Gyr	Lower confidence interval RC age
E_upper_age_rc	Gyr	Upper confidence interval RC age
Teff_diff	K	Difference in Effective Temperature (xgboost – rgb)
Flag	None	Marked 0 if model fit is converged

scope of this study. We also do not compute ages for stars above $3M_\odot$, which make up 1696 stars (or 1.26%) of our sample, as our investigation into these outliers leads to the conclusion that these mass values are overestimated and the majority of these objects are not truly young stars.

For each star we calculate its age in 3 different ways:

1. We assume that the stars are all RGB without introducing mass loss, or simply (current mass = birth mass).
2. We assume all stars are clump stars and adopt our empirical mass loss prescription.
3. We assume all stars are clump stars and adopt our theoretical mass loss prescription.

We present our final converged ages and determined evolutionary states in Table 2, along with an alternative list of available variables in Table 3. This comprehensive dataset is structured to allow future users the flexibility to reclassify evolutionary states or apply alternative classification schemes based on their own goals. Vari-

ables ending in “rgb” correspond to values calculated under the assumption that the star is on the red giant branch, while those ending in “rc” reflect calculations assuming the star is in the red clump. The final adopted evolutionary state for each star is indicated in the “Star_Type” column; however, both sets of variables are included in the dataset to allow for flexible reanalysis and completeness.

5. MASS LOSS

Mass loss occurs before stars reach the red clump, which means that the current mass of clump stars is not their birth mass. If this mass loss is not properly accounted for, it can introduce significant errors in age estimates.

5.1. Mass Loss Prescriptions

There are two general approaches for estimating mass loss: one is derived directly from the model tracks, and the other comes from empirical calibrations. The models

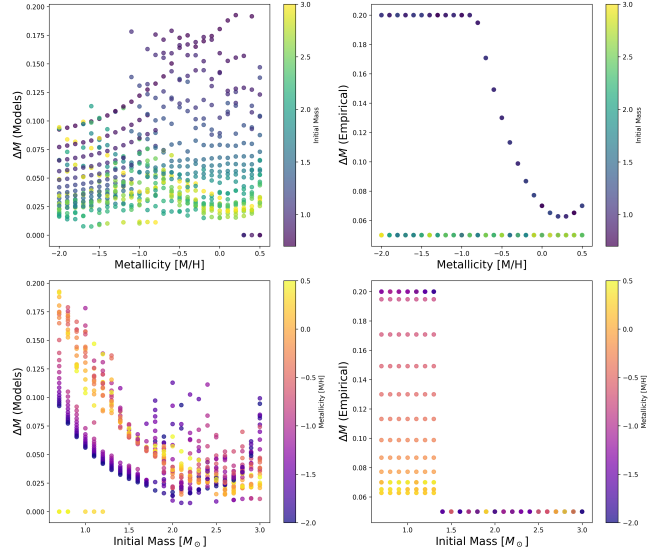


Figure 4. Predicted mass loss as a function of stellar mass and metallicity. The figure compares two mass loss schemes: one based on theoretical model tracks and the other using empirical mass loss calibrations from (Tayar et al. 2023) and (Pinsonneault et al. 2025). While theoretical predictions have a strong mass dependence and a weak metallicity dependence, the current empirical mapping is the opposite. We expect real mass loss rates to depend on both mass and metallicity. Therefore we compute ages with both sets of assumptions.

are calculated using prescriptions of mass loss that scale with the atmospheric properties (e.g. Reimers 1975), while empirical calibrations are based on observed data from different stars in the same environment.

For our analysis, we explored two options for mass loss: (1) Model-based which calculates mass loss based on the theoretical model tracks in our grid ($\eta_{\text{Reimers}} = 0.2$, Miglio et al. 2012), and (2) empirically-calibrated mass loss, which uses the difference in asteroseismic mass between α -enhanced RGB and clump stars to estimate a metallicity dependence to the mass loss, as described in the alternative age inference method from Pinsonneault et al. (2025) (see also Tayar et al. 2023). We show the predicted mass loss from these two schemes as a function of mass and metallicity in Figure 4.

Both methods have limitations. Empirical mass-loss trends have to be extrapolated to predict regions outside their initial calibration, and in this case this seems likely to overestimate the mass loss at low metallicity and high mass. On the other hand, the theoretical mass loss from the tracks exhibits a different metallicity trend that is inconsistent with observational data (Tailo et al. 2022; Howell et al. 2022; Pinsonneault et al. 2025; Marasco et al. 2025). For our main table, we decided to use the empirically-calibrated mass loss to better capture

the metallicity dependence, but we added an additional mass dependence calibrated on the models within our grid to better account for the expected and observed mass-dependence of red giant branch mass loss. For our empirical mass loss, we used the following equation from Pinsonneault et al. (2025) and applied it to all stars within our dataset:

$$\Delta_{\text{mass}} = (0.12 \cdot ([\text{M}/\text{H}] + 1.0)^2 + 0.95) - (0.3 \cdot [\text{M}/\text{H}] + 1.0)$$

We limited the value for mass loss to a maximum of 0.2 and applied a value of 0.05 for the value Δ_M in any star with a mass greater than 1.3 solar mass, coinciding with accepted expectations for mass loss (Pinsonneault et al. 2025).

For our theoretical prescription, we identified the track closest to the current mass and metallicity of each star in our dataset, and calculated a Δ_M for each of these stars according to the inferred mass expected on the red giant branch for a star of that mass and metallicity.

Because both mass loss and evolutionary state identification are uncertain (see Section 5), Table 2 provides ages inferred using our empirically calibrated mass loss, as well as ages calculated with no mass loss, allowing the reader to make alternative choices if desired.

5.2. Evolutionary State Identification

Because the amount of mass loss that has happened by the red clump is significant, and the amount of mass loss that has happened on the early part of the first ascent red giant branch is insignificant, it is important that we determine which stars are on the RGB and which are in the clump. Unfortunately, in the masses and metallicities of our sample, there is significant overlap between these two populations in temperature and gravity. Therefore, to differentiate them we use the temperatures expected for a first ascent red giant in our models for each star's mass, metallicity, and surface gravity compared to its observed temperature to determine if the temperature is more similar to a red giant of this mass, or more similar to a core-helium burning clump star. Specifically, for each star, we define “ $\text{Teff}_{\text{Diff}}$ ”, which is $T_{\text{Star}} - T_{\text{Model}}$ (see Bovy et al. 2012; Tayar et al. 2017; Holtzman et al. 2018; Vrard et al. 2024 for similar implementations). We show in Figure 5 that the distribution of $\text{Teff}_{\text{Diff}}$ has two clear peaks at 45 K and 208 K. The peak close to zero offset from the expected red giant branch temperature represents our red giants, while the peak around 200 K represents red clump stars, which are expected to be hotter than first ascent giants of the same mass. While there is clearly overlap between the clump and giant populations, we choose to divide them at a

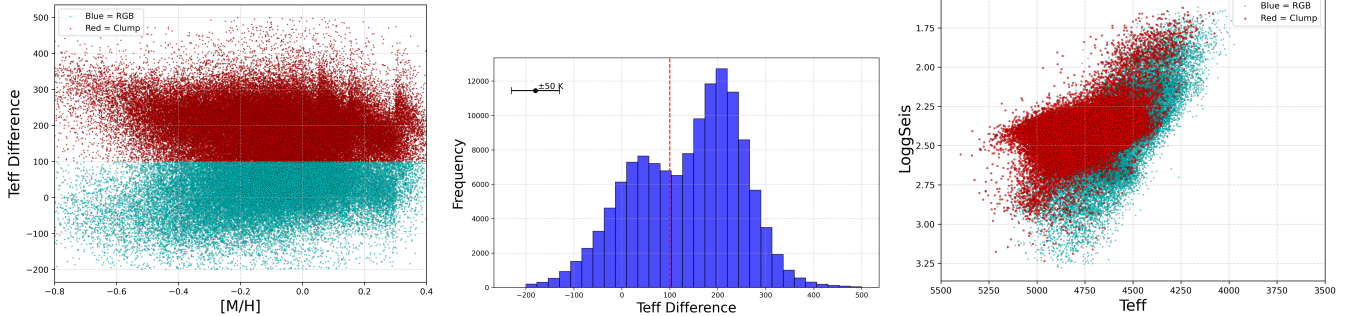


Figure 5. Effective Temperature Comparison and Metallicity Dependence. **Left:** Comparison of the derived effective temperatures (T_{eff}) with reference values ($T_{\text{eff, ref}}$) as a function of metallicity ($[\text{Fe}/\text{H}]$). Stars with differences above 100K were assumed to be red clump stars. **Middle Panel:** Histogram of the differences between derived and reference effective temperatures ($\Delta T_{\text{eff}} = T_{\text{eff}} - T_{\text{eff, ref}}$). A dashed vertical line is plotted at $\Delta T_{\text{eff}} = 100$ K, representing the chosen cutoff to ensure a clean sample of red giant branch (RGB) stars. The cross in the center histogram represents the average uncertainty of our Teff difference value. **Right:** Final Hertzsprung-Russell (HR) diagram showing the identified red giant branch (RGB) stars in blue and red clump (RC) stars in red. The RC stars are clearly separated from the RGB population, with the distinct “clump” feature visible around $\log g \approx 2.5$ and $T_{\text{eff}} \approx 4750$ K.

temperature offset of 100K, which is chosen to provide a purer sample of red giant stars. While other studies may adopt different cutoff values depending on their scientific goals, we find that $\Delta T_{\text{eff}} = 100$ K provides a suitable balance for our analysis, prioritizing the precision of RGB stellar parameters and ages. We note that varying the temperature of the division by < 15 K alters the sample distribution by roughly 2%, and we provide ages for each star based on evolutionary state in Table 2.

6. AGE DISTRIBUTIONS

Figure 6 presents a comparison of the asteroseismic age distributions for Red Giant Branch (RGB) and Clump stars observed by the TESS and Kepler missions (Pinsonneault et al. 2025). The histograms are divided into four panels, with the top row showing TESS data and the bottom row showing Kepler (APOKASC-3) data. Each row is further divided into RGB stars (left) and Clump stars (right), with ages limited to 0–13.8 Gyr to focus on physically plausible stellar ages.

Both TESS and Kepler show similar age distributions for RGB and Clump stars, with peaks in the age histograms occurring at comparable values. This suggests that the stellar populations observed by both missions share common characteristics. The general agreement between the two datasets indicates that age determination methods are consistent across missions, despite differences in observational strategies and target selection. This agreement further supports the robustness of the age estimation methods used in our TESS sample.

The TESS sample is significantly larger, with the number of stars in individual bins ranging up to 3000 for RGB stars and 5000 for Clump stars. In contrast, the

Kepler sample is much smaller, with the y-axis limited to 1000 stars for both RGB and Clump populations. This difference in sample size reflects the broader sky coverage of TESS compared to Kepler, which observed a smaller, fixed region of the sky. Kepler’s targets are primarily just above the galactic disk, while TESS includes stars from a wider range of galactic latitudes, potentially sampling different stellar populations, leading to shifts in the overall distribution. TESS captures more of the sky including the galactic plane, resulting in a higher percentage of younger stars observed. In contrast, Kepler observes farther away and therefore sees a higher fraction of old stars from the thick disk and halo.

Both datasets (red giant and clump) show a small fraction (4045/132794) of stars with ages exceeding the age of the universe (13.8 Gyr). These outliers may result from uncertainties in age determination or systematic biases in the stellar models used. They also could be the result of binary interactions. Close binaries are more common at low metallicities and higher masses (Moe & Di Stefano 2017; Moe et al. 2019) and some of these old stars, especially in the clump, may represent the remains of stars that have undergone significant envelope stripping (Li et al. 2022). We do not classify any of our stars as potential binary interaction products in our sample, but we note that some of the most extreme outliers may warrant further investigation as candidate binary remnants. Future studies incorporating binary evolution models or additional photometric and spectroscopic diagnostics could provide valuable insights into the nature of these anomalous stars.

Figure 7 shows the age-metallicity distribution for our entire sample of stars, including both Red Giant Branch (RGB) and Red Clump (RC) populations. The plot re-

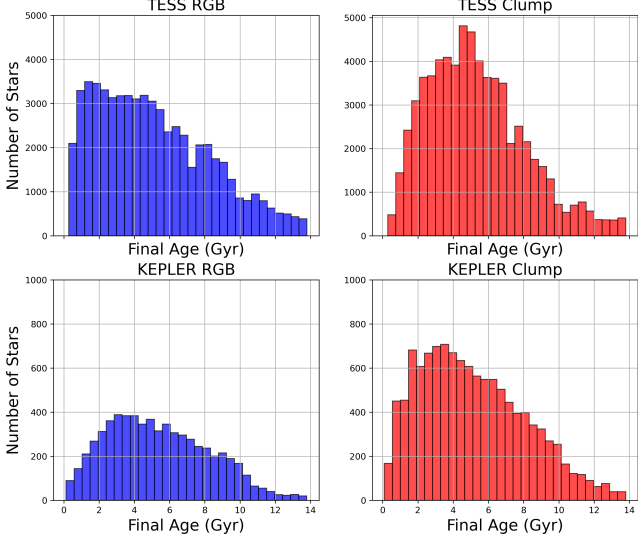


Figure 6. Comparison of age distributions for Red Giant Branch (RGB) and Clump stars observed by TESS (top row) and Kepler (bottom row), divided into four panels with ages limited to the age of the universe. Both missions show similar age trends, with TESS samples being significantly larger than Kepler’s. Small variances may arise from differences in sky coverage and observation periods.

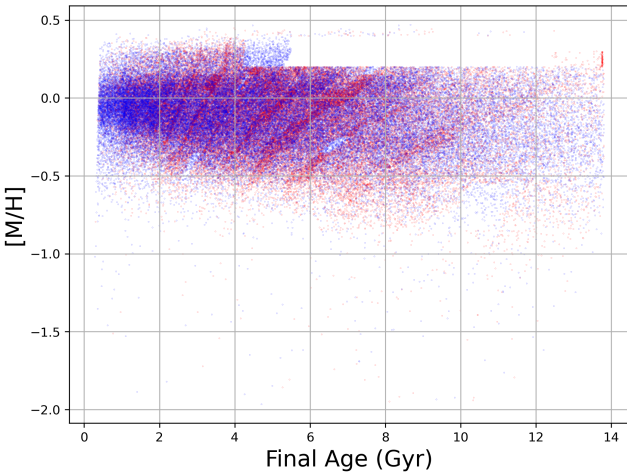


Figure 7. Age-metallicity distribution for the entire sample of stars, including Red Giant Branch (blue) and Red Clump (red) populations. The “striping” effect is has two sources: the weights assigned during linear interpolation being biased toward the lower mass track, and from the structure introduced from the mass loss calculations (see text). The rectangular gap at higher metallicities and old ages reflects missing or incomplete models in our grid.

veals a distinct “striping” pattern, which arises from two sources. First, the structure introduced by the mass loss calculation (see Section 5). Second, the weights assigned during linear interpolation are biased toward the lower-

mass track (see Section 4). This clustering highlights the sensitivity of the determined ages to the methodology and grid being used. To mitigate the striping effect, future work could explore increasing the number of interpolation steps or having a more robust mass range with even smaller mass increments.

Additionally, the plot exhibits a rectangular gap at higher metallicities, which arises from models that failed to run to completion at higher metallicities, leading to gaps in the distribution. In order to account for the model-to-model systematic differences in inferred ages depending on the model grid used (Tayar et al. 2022; Pinsonneault et al. 2025; Morales et al. 2025), we have added an additional 10% systematic age uncertainty in quadrature to the observational uncertainties computed using the mass, surface gravity, and metallicity uncertainties. Previous work has suggested that this is a representative value for model-to-model absolute age differences for stars in this regime (Morales et al. 2025). Even with the aforementioned caveats, we feel that our ages are still valuable because of their large number, and homogeneously derived nature. Despite these minor challenges, the overall distribution of ages has similar trends to previous studies, and can therefore still be used in future work. We believe it can provide a useful dataset or training sample for a variety of future work.

7. DISCUSSION/CONCLUSIONS

In this work, we present a sample of ages that can be used for galactic archaeology. In particular:

- We demonstrated that data from *TESS* and *Gaia* can be effectively combined to estimate stellar masses for large samples of stars.
- Using this sample, we constructed a grid of stellar models specifically tailored to its properties. These models incorporate updated physics and are tuned to the range of masses and metallicities observed in our dataset.
- Leveraging these models, we estimated ages for 132,794 stars with an average uncertainty of <23%. This represents a significant step forward in the size of the stellar sample with asteroseismically-informed ages available.
- We quantified both the statistical and systematic uncertainties on our masses and inferred ages. On average, the combined uncertainties were 12% in mass and 23% in age.
- Our age estimates replicate the trends observed in previous works, validating both our methodology

and the model grid used in this study. Our results provide benchmarks for testing galaxy formation models and further our understanding of stellar evolution in low-mass stars.

- These results highlight the potential of such age estimates for applications in galactic archaeology, potentially facilitating new insights into the formation and evolutionary history of the Milky Way.

This study underscores the value of combining precise observational data with tailored theoretical models. By leveraging *TESS*'s extensive all-sky data and *Gaia*'s precise astrometric and photometric measurements, we addressed two of the major challenges in stellar age determination outlined in our introduction: limited generalizability of stellar samples and systematic discrepancies in age estimates due to model-dependent uncertainties. Specifically, we demonstrated that red giants with seismically inferred mass estimates can produce age estimates with an uncertainty of 23%, providing a useful sample for future galactic archaeology.

The results presented here not only validate the feasibility of extending precise age determinations to a much larger and more representative sample of the galaxy but also provide critical benchmarks for testing and refining models of the Milky Way's formation and evolution. Our work confirms trends observed in previous studies (e.g., Ness et al. 2016; Mackereth et al. 2018; Feuillet et al. 2022) and highlights the possibility of utilizing seismically-inferred masses and evolutionary states as a tool for age estimation in future work.

Moving forward, these techniques can be applied to explore additional stellar populations, such as those in the galactic halo or accreted dwarf galaxies, where precise ages could shed light on key questions about their formation and evolution (e.g., Helmi et al. 2018; Grunblatt et al. 2022). Moreover, extending these methods to low-metallicity populations or stars in more extreme environments could help refine our understanding of the interplay between the galaxy's components, as well as the role of accretion and interactions over cosmic time (Chaplin et al. 2020).

Future studies may also benefit from integrating asteroseismic techniques with machine learning approaches to further increase the precision and accessibility of stellar ages for even larger datasets (Ness et al. 2016; Mackereth et al. 2019). For example, by building on the machine learning methods validated on *Kepler* data (Queiroz et al. 2023; Stone-Martinez et al. 2024), we can optimize models for the broader and more diverse sample provided by *TESS*. This integration could also address the challenges of training sample reliance and edge-case inaccuracies, which remain limitations in current age estimation techniques (Mackereth et al. 2019; Tayar et al. 2023).

ACKNOWLEDGMENTS

A.T. acknowledges support from the University of Florida CLAS-Scholars and USP-Scholars programs. A.T., L.M., and J.T. acknowledge support from 80NSSC22K0812. A.T. and J.T. acknowledge support from 80NSSC23K0436. We thank Z. Claytor for helpful discussions about kiauhoku and M. Joyce for providing her MESA input files.

A.T. Thanks Georgios and Hatice Theodoridis for helpful discussions and support.

REFERENCES

- Abdurro'uf, Accetta, K., Aerts, C., et al. 2022, ApJS, 259, 35, doi: [10.3847/1538-4365/ac4414](https://doi.org/10.3847/1538-4365/ac4414)
- Anders, F., Gispert, P., Ratcliffe, B., et al. 2023, A&A, 678, A158, doi: [10.1051/0004-6361/202346666](https://doi.org/10.1051/0004-6361/202346666)
- Andrae, R., Rix, H.-W., & Chandra, V. 2023, ApJS, 267, 8, doi: [10.3847/1538-4365/acd53e](https://doi.org/10.3847/1538-4365/acd53e)
- Bahcall, J. N., Serenelli, A. M., & Basu, S. 2006, ApJS, 165, 400, doi: [10.1086/504043](https://doi.org/10.1086/504043)
- Berger, T. A., Huber, D., van Saders, J. L., et al. 2020, AJ, 159, 280, doi: [10.3847/1538-3881/159/6/280](https://doi.org/10.3847/1538-3881/159/6/280)
- Berger, T. A., Schlieder, J. E., & Huber, D. 2023, arXiv e-prints, arXiv:2301.11338, doi: [10.48550/arXiv.2301.11338](https://doi.org/10.48550/arXiv.2301.11338)
- Bloecker, T. 1995, A&A, 297, 727
- Borucki, W. J., Koch, D., Basri, G., et al. 2010, Science, 327, 977, doi: [10.1126/science.1185402](https://doi.org/10.1126/science.1185402)
- Bovy, J., Rix, H.-W., & Hogg, D. W. 2012, ApJ, 751, 131, doi: [10.1088/0004-637X/751/2/131](https://doi.org/10.1088/0004-637X/751/2/131)
- Brown, T. M., Gilliland, R. L., Noyes, R. W., & Ramsey, L. W. 1991, ApJ, 368, 599, doi: [10.1086/169725](https://doi.org/10.1086/169725)
- Byrom, S., & Tayar, J. 2024, Research Notes of the American Astronomical Society, 8, 201, doi: [10.3847/2515-5172/ad7093](https://doi.org/10.3847/2515-5172/ad7093)
- Chaplin, W. J., Serenelli, A. M., Miglio, A., et al. 2020, Nature Astronomy, 4, 382, doi: [10.1038/s41550-019-0975-9](https://doi.org/10.1038/s41550-019-0975-9)

- Chen, Y.-Q., Zhao, G., Liu, C., et al. 2015, Research in Astronomy and Astrophysics, 15, 1125, doi: [10.1088/1674-4527/15/8/003](https://doi.org/10.1088/1674-4527/15/8/003)
- Choi, J., Dotter, A., Conroy, C., et al. 2016, ApJ, 823, 102, doi: [10.3847/0004-637X/823/2/102](https://doi.org/10.3847/0004-637X/823/2/102)
- Chugunov, A. I., Dewitt, H. E., & Yakovlev, D. G. 2007, PhRvD, 76, 025028, doi: [10.1103/PhysRevD.76.025028](https://doi.org/10.1103/PhysRevD.76.025028)
- Claytor, Z. R., van Saders, J. L., Santos, Á. R. G., et al. 2020, ApJ, 888, 43, doi: [10.3847/1538-4357/ab5c24](https://doi.org/10.3847/1538-4357/ab5c24)
- Dotter, A. 2016, ApJS, 222, 8, doi: [10.3847/0007-0049/222/1/8](https://doi.org/10.3847/0007-0049/222/1/8)
- Eddington, A. S. 1930, MNRAS, 90, 668, doi: [10.1093/mnras/90.7.668](https://doi.org/10.1093/mnras/90.7.668)
- Ferguson, J. W., Alexander, D. R., Allard, F., et al. 2005, ApJ, 623, 585, doi: [10.1086/428642](https://doi.org/10.1086/428642)
- Feuillet, D. K., Feltzing, S., Sahlholdt, C., & Bensby, T. 2022, ApJ, 934, 21, doi: [10.3847/1538-4357/ac76ba](https://doi.org/10.3847/1538-4357/ac76ba)
- Gaia Collaboration. 2022, VizieR Online Data Catalog: Gaia DR3 Part 1. Main source (Gaia Collaboration, 2022), VizieR On-line Data Catalog: I/355. Originally published in: doi:10.1051/0004-63, doi: [10.26093/cds/vizier.1355](https://doi.org/10.26093/cds/vizier.1355)
- Gaia Collaboration, Prusti, T., de Bruijne, J. H. J., et al. 2016, A&A, 595, A1, doi: [10.1051/0004-6361/201629272](https://doi.org/10.1051/0004-6361/201629272)
- Gaia Collaboration, Brown, A. G. A., Vallenari, A., et al. 2018, A&A, 616, A1, doi: [10.1051/0004-6361/201833051](https://doi.org/10.1051/0004-6361/201833051)
- . 2021, A&A, 649, A1, doi: [10.1051/0004-6361/202039657](https://doi.org/10.1051/0004-6361/202039657)
- García Pérez, A. E., Allende Prieto, C., Holtzman, J. A., et al. 2016, AJ, 151, 144, doi: [10.3847/0004-6256/151/6/144](https://doi.org/10.3847/0004-6256/151/6/144)
- Godoy-Rivera, D., Pinsonneault, M. H., & Rebull, L. M. 2021, ApJS, 257, 46, doi: [10.3847/1538-4365/ac2058](https://doi.org/10.3847/1538-4365/ac2058)
- Grevesse, N., & Sauval, A. J. 1998, SSRv, 85, 161, doi: [10.1023/A:1005161325181](https://doi.org/10.1023/A:1005161325181)
- Grunblatt, S. K., Saunders, N., Sun, M., et al. 2022, AJ, 163, 120, doi: [10.3847/1538-3881/ac4972](https://doi.org/10.3847/1538-3881/ac4972)
- Hatt, E., Nielsen, M. B., Chaplin, W. J., et al. 2022, VizieR Online Data Catalog: Solar-like oscillators catalogue (Hatt+, 2023), VizieR On-line Data Catalog: J/A+A/669/A67. Originally published in: 2023A&A...669A..67H, doi: [10.26093/cds/vizier.36690067](https://doi.org/10.26093/cds/vizier.36690067)
- Hatt, E. J., Ong, J. M. J., Nielsen, M. B., et al. 2024, MNRAS, 534, 1060, doi: [10.1093/mnras/stae2053](https://doi.org/10.1093/mnras/stae2053)
- Helmi, A., Babusiaux, C., Koppelman, H. H., et al. 2018, Nature, 563, 85, doi: [10.1038/s41586-018-0625-x](https://doi.org/10.1038/s41586-018-0625-x)
- Henyey, L. G., Forbes, J. E., & Gould, N. L. 1964, ApJ, 139, 306, doi: [10.1086/147754](https://doi.org/10.1086/147754)
- Holtzman, J. A., Shetrone, M., Johnson, J. A., et al. 2015, AJ, 150, 148, doi: [10.1088/0004-6256/150/5/148](https://doi.org/10.1088/0004-6256/150/5/148)
- Holtzman, J. A., Hasselquist, S., Shetrone, M., et al. 2018, AJ, 156, 125, doi: [10.3847/1538-3881/aad4f9](https://doi.org/10.3847/1538-3881/aad4f9)
- Hon, M., Stello, D., & Yu, J. 2018, MNRAS, 476, 3233, doi: [10.1093/mnras/sty483](https://doi.org/10.1093/mnras/sty483)
- Hon, M., Huber, D., Kuszlewicz, J. S., et al. 2021, ApJ, 919, 131, doi: [10.3847/1538-4357/ac14b1](https://doi.org/10.3847/1538-4357/ac14b1)
- Howell, M., Campbell, S. W., Stello, D., & De Silva, G. M. 2022, MNRAS, 515, 3184, doi: [10.1093/mnras/stac1918](https://doi.org/10.1093/mnras/stac1918)
- Huang, C. X., Vanderburg, A., Pál, A., et al. 2020, Research Notes of the American Astronomical Society, 4, 206, doi: [10.3847/2515-5172/abca2d](https://doi.org/10.3847/2515-5172/abca2d)
- Hubeny, I., Allende Prieto, C., Osorio, Y., & Lanz, T. 2021, arXiv e-prints, arXiv:2104.02829, doi: [10.48550/arXiv.2104.02829](https://doi.org/10.48550/arXiv.2104.02829)
- Hubeny, I., & Lanz, T. 2017, arXiv e-prints, arXiv:1706.01859, doi: [10.48550/arXiv.1706.01859](https://doi.org/10.48550/arXiv.1706.01859)
- Huber, D., Bedding, T. R., Stello, D., et al. 2011, ApJ, 743, 143, doi: [10.1088/0004-637X/743/2/143](https://doi.org/10.1088/0004-637X/743/2/143)
- Huber, D., Zinn, J., Bojsen-Hansen, M., et al. 2017, ApJ, 844, 102, doi: [10.3847/1538-4357/aa75ca](https://doi.org/10.3847/1538-4357/aa75ca)
- Iglesias, C. A., & Rogers, F. J. 1996, ApJ, 464, 943, doi: [10.1086/177381](https://doi.org/10.1086/177381)
- Iorio, G., Belokurov, V., Erkal, D., et al. 2018, MNRAS, 474, 2142, doi: [10.1093/mnras/stx2819](https://doi.org/10.1093/mnras/stx2819)
- Jermyn, A. S., Bauer, E. B., Schwab, J., et al. 2023, ApJS, 265, 15, doi: [10.3847/1538-4365/aca8ed](https://doi.org/10.3847/1538-4365/aca8ed)
- Jönsson, H., Allende Prieto, C., Holtzman, J. A., et al. 2018, AJ, 156, 126, doi: [10.3847/1538-3881/aad4f5](https://doi.org/10.3847/1538-3881/aad4f5)
- Jönsson, H., Holtzman, J. A., Allende Prieto, C., et al. 2020, AJ, 160, 120, doi: [10.3847/1538-3881/aba592](https://doi.org/10.3847/1538-3881/aba592)
- Joyce, M., & Chaboyer, B. 2018, ApJ, 864, 99, doi: [10.3847/1538-4357/aad464](https://doi.org/10.3847/1538-4357/aad464)
- Joyce, M., Johnson, C. I., Marchetti, T., et al. 2023, ApJ, 946, 28, doi: [10.3847/1538-4357/acb692](https://doi.org/10.3847/1538-4357/acb692)
- Joyce, M., Molnár, L., Cinquegrana, G., et al. 2024, ApJ, 971, 186, doi: [10.3847/1538-4357/ad534a](https://doi.org/10.3847/1538-4357/ad534a)
- Kjeldsen, H., & Bedding, T. R. 1995, A&A, 293, 87, doi: [10.48550/arXiv.astro-ph/9403015](https://doi.org/10.48550/arXiv.astro-ph/9403015)
- Kunz, R., Fey, M., Jaeger, M., et al. 2002, ApJ, 567, 643, doi: [10.1086/338384](https://doi.org/10.1086/338384)
- Leung, H. W., & Bovy, J. 2019, Monthly Notices of the Royal Astronomical Society, 489, 2079–2096, doi: [10.1093/mnras/stz2245](https://doi.org/10.1093/mnras/stz2245)
- Li, Y., Bedding, T. R., Murphy, S. J., et al. 2022, Nature Astronomy, 6, 673–680, doi: [10.1038/s41550-022-01648-5](https://doi.org/10.1038/s41550-022-01648-5)
- Lund, M. N., Silva Aguirre, V., Davies, G. R., et al. 2017, ApJ, 835, 172, doi: [10.3847/1538-4357/835/2/172](https://doi.org/10.3847/1538-4357/835/2/172)

- Mackereth, J. T., Bovy, J., Schiavon, R. P., & SDSS-IV/APOGEE Collaboration. 2018, in IAU Symposium, Vol. 334, Rediscovering Our Galaxy, ed. C. Chiappini, I. Minchev, E. Starkenburg, & M. Valentini, 265–268, doi: [10.1017/S1743921317006627](https://doi.org/10.1017/S1743921317006627)
- Mackereth, J. T., Bovy, J., Leung, H. W., et al. 2019, MNRAS, 489, 176, doi: [10.1093/mnras/stz1521](https://doi.org/10.1093/mnras/stz1521)
- Mackereth, J. T., Miglio, A., Elsworth, Y., et al. 2021, MNRAS, 502, 1947, doi: [10.1093/mnras/stab098](https://doi.org/10.1093/mnras/stab098)
- Majewski, S. R., Schiavon, R. P., Frinchaboy, P. M., et al. 2017, AJ, 154, 94, doi: [10.3847/1538-3881/aa784d](https://doi.org/10.3847/1538-3881/aa784d)
- Marasco, C., Tayar, J., & Nidever, D. 2025, AJ, Submitted
- Marigo, P., & Aringer, B. 2009, A&A, 508, 1539, doi: [10.1051/0004-6361/200912598](https://doi.org/10.1051/0004-6361/200912598)
- Miglio, A., Brogaard, K., Stello, D., et al. 2012, MNRAS, 419, 2077, doi: [10.1111/j.1365-2966.2011.19859.x](https://doi.org/10.1111/j.1365-2966.2011.19859.x)
- Moe, M., & Di Stefano, R. 2017, ApJS, 230, 15, doi: [10.3847/1538-4365/aa6fb6](https://doi.org/10.3847/1538-4365/aa6fb6)
- Moe, M., Kratter, K. M., & Badenes, C. 2019, ApJ, 875, 61, doi: [10.3847/1538-4357/ab0d88](https://doi.org/10.3847/1538-4357/ab0d88)
- Morales, L., Tayar, J., & Claytor, Z. 2025, AJ, Submitted
- Nataf, D. M., Schlaufman, K. C., Reggiani, H., & Hahn, I. 2024, ApJ, 976, 87, doi: [10.3847/1538-4357/ad7c4e](https://doi.org/10.3847/1538-4357/ad7c4e)
- Nelder, J. A., & Mead, R. 1965, The Computer Journal, 7, 308, doi: [10.1093/comjnl/7.4.308](https://doi.org/10.1093/comjnl/7.4.308)
- Ness, M., Hogg, D. W., Rix, H. W., et al. 2016, ApJ, 823, 114, doi: [10.3847/0004-637X/823/2/114](https://doi.org/10.3847/0004-637X/823/2/114)
- Paxton, B., Bildsten, L., Dotter, A., et al. 2011, ApJS, 192, 3, doi: [10.1088/0067-0049/192/1/3](https://doi.org/10.1088/0067-0049/192/1/3)
- Paxton, B., Cantiello, M., Arras, P., et al. 2013, ApJS, 208, 4, doi: [10.1088/0067-0049/208/1/4](https://doi.org/10.1088/0067-0049/208/1/4)
- Paxton, B., Marchant, P., Schwab, J., et al. 2015, ApJS, 220, 15, doi: [10.1088/0067-0049/220/1/15](https://doi.org/10.1088/0067-0049/220/1/15)
- Paxton, B., Schwab, J., Bauer, E. B., et al. 2018, ApJS, 234, 34, doi: [10.3847/1538-4365/aaa5a8](https://doi.org/10.3847/1538-4365/aaa5a8)
- Paxton, B., Smolec, R., Schwab, J., et al. 2019, ApJS, 243, 10, doi: [10.3847/1538-4365/ab2241](https://doi.org/10.3847/1538-4365/ab2241)
- Pinsonneault, M. H., Zinn, J. C., Tayar, J., et al. 2025, ApJS, 276, 69, doi: [10.3847/1538-4365/ad9fef](https://doi.org/10.3847/1538-4365/ad9fef)
- Planck Collaboration, Aghanim, N., Akrami, Y., et al. 2020, A&A, 641, A6, doi: [10.1051/0004-6361/201833910](https://doi.org/10.1051/0004-6361/201833910)
- Prša, A., Harmanec, P., Torres, G., et al. 2016, AJ, 152, 41, doi: [10.3847/0004-6256/152/2/41](https://doi.org/10.3847/0004-6256/152/2/41)
- Queiroz, A. B. A., Anders, F., Chiappini, C., et al. 2023, A&A, 673, A155, doi: [10.1051/0004-6361/202245399](https://doi.org/10.1051/0004-6361/202245399)
- Reimers, D. 1975, Memoires of the Societe Royale des Sciences de Liege, 8, 369
- Ricker, G. R., Latham, D. W., Vanderspek, R. K., et al. 2010, in American Astronomical Society Meeting Abstracts, Vol. 215, American Astronomical Society Meeting Abstracts #215, 450.06
- Rogers, F. J., Swenson, F. J., & Iglesias, C. A. 1996, ApJ, 456, 902, doi: [10.1086/176705](https://doi.org/10.1086/176705)
- Schonhet-Stasik, J., Zinn, J., Stassun, K., et al. 2023, in American Astronomical Society Meeting Abstracts, Vol. 242, American Astronomical Society Meeting Abstracts, 120.08
- Silva Aguirre, V., Bojsen-Hansen, M., Slumstrup, D., et al. 2018, MNRAS, 475, 5487, doi: [10.1093/mnras/sty150](https://doi.org/10.1093/mnras/sty150)
- Sinha, A., Zasowski, G., Frinchaboy, P., et al. 2024, ApJ, 975, 89, doi: [10.3847/1538-4357/ad78e1](https://doi.org/10.3847/1538-4357/ad78e1)
- Stassun, K. G., Oelkers, R. J., Paegert, M., et al. 2019, AJ, 158, 138, doi: [10.3847/1538-3881/ab3467](https://doi.org/10.3847/1538-3881/ab3467)
- Stello, D., Bruntt, H., Preston, H., & Buzasi, D. 2008, ApJL, 674, L53, doi: [10.1086/528936](https://doi.org/10.1086/528936)
- Stello, D., Saunders, N., Grunblatt, S., et al. 2022, Monthly Notices of the Royal Astronomical Society, 512, 1677, doi: [10.1093/mnras/stac414](https://doi.org/10.1093/mnras/stac414)
- Stokholm, A., Aguirre Børnsen-Koch, V., Stello, D., Hon, M., & Reyes, C. 2023, MNRAS, 524, 1634, doi: [10.1093/mnras/stad1912](https://doi.org/10.1093/mnras/stad1912)
- Stone-Martinez, A., Holtzman, J. A., Imig, J., et al. 2024, AJ, 167, 73, doi: [10.3847/1538-3881/ad12a6](https://doi.org/10.3847/1538-3881/ad12a6)
- Tailo, M., Corsaro, E., Miglio, A., et al. 2022, A&A, 662, L7, doi: [10.1051/0004-6361/202243721](https://doi.org/10.1051/0004-6361/202243721)
- Takeda, G., Ford, E. B., Sills, A., et al. 2007, ApJS, 168, 297, doi: [10.1086/509763](https://doi.org/10.1086/509763)
- Tayar, J., Claytor, Z. R., Huber, D., & van Saders, J. 2022, ApJ, 927, 31, doi: [10.3847/1538-4357/ac4bbc](https://doi.org/10.3847/1538-4357/ac4bbc)
- Tayar, J., & Joyce, M. 2025, arXiv e-prints, arXiv:2502.09582, doi: [10.48550/arXiv.2502.09582](https://doi.org/10.48550/arXiv.2502.09582)
- Tayar, J., Somers, G., Pinsonneault, M. H., et al. 2017, ApJ, 840, 17, doi: [10.3847/1538-4357/aa6a1e](https://doi.org/10.3847/1538-4357/aa6a1e)
- Tayar, J., Claytor, Z. R., Fox, Q., et al. 2023, Research Notes of the American Astronomical Society, 7, 273, doi: [10.3847/2515-5172/ad16d3](https://doi.org/10.3847/2515-5172/ad16d3)
- Theodoridis, A. T., & Tayar, J. 2023, Research Notes of the AAS, 7, 148, doi: [10.3847/2515-5172/ace7af](https://doi.org/10.3847/2515-5172/ace7af)
- Ting, Y.-S. 2024, arXiv e-prints, arXiv:2412.05806, doi: [10.48550/arXiv.2412.05806](https://doi.org/10.48550/arXiv.2412.05806)
- van Saders, J. L., & Pinsonneault, M. H. 2013, ApJ, 776, 67, doi: [10.1088/0004-637X/776/2/67](https://doi.org/10.1088/0004-637X/776/2/67)
- Vrard, M., Pinsonneault, M. H., Elsworth, Y., et al. 2024, arXiv e-prints, arXiv:2411.03101, doi: [10.48550/arXiv.2411.03101](https://doi.org/10.48550/arXiv.2411.03101)
- Xiang, M., & Rix, H.-W. 2022, Nature, 603, 599, doi: [10.1038/s41586-022-04496-5](https://doi.org/10.1038/s41586-022-04496-5)

Ying, J. M., Chaboyer, B., Boudreault, E. M., et al. 2023,
AJ, 166, 18, doi: [10.3847/1538-3881/acd9b1](https://doi.org/10.3847/1538-3881/acd9b1)
Zhou, J., Bi, S., Yu, J., et al. 2024, ApJS, 271, 17,
doi: [10.3847/1538-4365/ad18db](https://doi.org/10.3847/1538-4365/ad18db)

Zinn, J. C., Pinsonneault, M. H., Huber, D., & Stello, D.
2019, ApJ, 878, 136, doi: [10.3847/1538-4357/ab1f66](https://doi.org/10.3847/1538-4357/ab1f66)

8. APPENDIX A

Table 3. Table of our collected data and computed values including spectroscopic, Gaia-derived, and asteroseismic results, as well as derived masses and ages (see text for details) assuming our alternate, model-based mass loss scheme for red clump stars. This table is available in its entirety in machine-readable form in the online article and on [Zenodo](#).

Label	Units	Contents
TIC	None	Stellar ID in TESS
Star_type	None	Recommended Evolutionary State
Final_age	Gyr	Age based on evolutionary state
ν_{max}	μHz	Frequency of Maximum power, Hon et al. 2021
Radius_gaia	R_{\odot}	Radius from Gaia, Hon et al. 2021
Teff_xgboost	K	T_{eff} from Gaia XGBoost
M_H_xgboost	dex	[Fe/H] metallicity from Gaia XGBoost
Logg_xgboost	cgs	Spectroscopic logg from XGBoost
Logg_seis	cgs	Seismic logg
E_Logg_seis	cgs	Uncertainty on seismic logg
Mass_seis	M_{\odot}	Seismic Mass
E_Mass_seis	M_{\odot}	Uncertainty on seismic mass
Initial_mass	M_{\odot}	Assumed initial mass of star accounting for model-derived mass loss
Teff_rgb	K	Model temperature assuming RGB
Teff_rc	K	Model temperature assuming RGB
Mean_age_rgb	Gyr	Mean age assuming RGB
Mean_age_rc	Gyr	Mean age assuming RC
Median_age_rgb	Gyr	Median age assuming RGB
Median_age_rc	Gyr	Median age assuming RC
E_age_rgb	Gyr	Standard deviation on RGB age
E_age_rc	Gyr	Standard deviation on RC age
E_lower_age_rgb	Gyr	Lower confidence interval RGB age
E_upper_age_rgb	Gyr	Upper confidence interval RGB age
E_lower_age_rc	Gyr	Lower confidence interval RC age
E_upper_age_rc	Gyr	Upper confidence interval RC age
Teff_diff	K	Difference in Effective Temperature (xgboost – rgb)
Flag	None	Marked 0 if model fit is converged

APPENDIX B: MESA INLIST SOLAR CONFIGURATION

Inlist_common file used for solar calibrated MESA modeling. Please view documentation for complete process on MESA modelling. This file is available in its entirety in machine-readable form in the online article and on [Zenodo](#).

```
!!!!!!!!!!!!!!!!!!!!!!!!!!!!!!!
!
! authors: A. Theodoridis based on inlist from G. C. Cinquegrana & M. Joyce
!
!!!!!!!!!!!!!!!!!!!!!!!!!!!!!!!

&star_job
    history_columns_file = 'history_columns.list'
    profile_columns_file = 'profile_columns.list'

    save_model_when_terminate = .true.
    save_model_filename = 'final.model'

    change_initial_net = .true. ! switch nuclear reaction network
    new_net_name = 'pp_and_cno_extras.net'

    set_initial_model_number = .true.
    initial_model_number = 0

    ! network

        auto_extend_net = .true.
        h_he_net = 'pp_extras.net' !'basic.net'
        co_net = 'co_burn.net'
        adv_net = 'approx21.net' !! unclear; do we need technetium? do we care?

        num_special_rate_factors = 1
        reaction_for_special_factor(1) = 'r_c12_ag_o16'
        special_rate_factor(1) = 1
        filename_of_special_rate(1) = 'r_c12_ag_o16_kunz.txt'

    ! opacities
        initial_zfracs = 3 ! for L03 solar scaling

/ !end of star_job namelist

&eos

/ ! end of eos namelist

&kap
    Zbase = 0.0179492d0 ! 0.03d0

    !! AESOPUS needs to be removed when Z = 0.02 or higher
```

```

use_Type2_opacities = .true.
kap_file_prefix = 'gs98'
kap_CO_prefix = 'gs98_co'

! kap_lowT_prefix = 'AESOPUS'
! AESOPUS_filename = 'AESOPUS_GCJul22_allZ.h5'
kap_lowT_prefix = 'lowT_fa05_gs98' !! for z= 0.02, 0.05

/ ! end of kap namelist

&controls

initial_mass = 1.0
initial_y = 0.2725693    !! probably fix
initial_z = 0.0179492 !0.03    !! loop

mixing_length_alpha = 1.94 !! from Giulia's solar calibration, so keep it
MLT_option = 'Henyey'

num_trace_history_values = 2
trace_history_value_name(1) = 'rel_E_err'
trace_history_value_name(2) = 'log_rel_run_E_err'

!! Artemis change for upper limit Log

!!log_L_upper_limit = 0

log_g_lower_limit = -1d99
log_g_upper_limit = 1d99

power_h_burn_upper_limit = 1d99

atm_option = 'T_tau'
atm_T_tau_relation = 'Eddington'
atm_T_tau_opacity = 'fixed'

cool_wind_RGB_scheme = 'Reimers'
cool_wind_AGB_scheme = 'Blocker'
RGB_to_AGB_wind_switch = 1d-4
Reimers_scaling_factor = 0.2d0
Blocker_scaling_factor = 0.01d0!0.01d0 !! eta_Bloecker

overshoot_scheme(1) = 'exponential'
overshoot_zone_type(1) = 'any'
overshoot_zone_loc(1) = 'core'
overshoot_bdy_loc(1) = 'any'
overshoot_f(1) = 0.016

```

```
overshoot_f0(1) = 0.004

overshoot_scheme(2) = 'exponential'
overshoot_zone_type(2) = 'any'
overshoot_zone_loc(2) = 'shell'
overshoot_bdy_loc(2) = 'any'
overshoot_f(2) = 0.0174
overshoot_f0(2) = 0.004

min_timestep_limit = 1d-4

!! testing whether this gets through TACHeB 7/18/23
energy_eqn_option = 'dedt' !! copy-pasted from 1.3M highZ test suite case 7/20/23
! use_gold2 tolerances = .true.
!! weakening tolerances
relax_use_gold_tolerances = .true.

use_Ledoux_criterion = .false.

photo_interval = -1 !100 !50 !! changed to 50
photo_digits = 5 !3

! if true, write out puls. infos when writing profile
write_profiles_flag = .true. !.true.
write_pulse_data_with_profile = .true. !.true.
pulse_data_format = 'GYRE'

/ ! end of controls namelist
```